AIAA JOURNAL
Vol. 49, No. 6, June 2011

Aerodynamic Characteristics at Low Reynolds Numbers for Wings of Various Planforms

M. Okamoto*
Kanazawa Institute of Technology, Nonoichi 921-8501, Japan
and
A. Azuma†
University of Tokyo, Kawasaki 212-0021, Japan

DOI: 10.2514/1.J050071

The aerodynamic characteristics of various wing planforms at low Reynolds numbers (about 1×10^4) were studied by conducting wind-tunnel tests. These low Reynolds numbers correspond to the flights of small creatures, such as insects. Elliptical, rectangular, and triangular planforms with various aspect ratios were used in this study, as well as a swept rectangular (parallelogram) wing with an aspect ratio of four. The wing sections of all models were thin rectangular airfoils. The aerodynamic forces (lift and drag) and the pitching moment acting on the wing were measured for a wide range of angles of attack (including the maximum of 90 deg). Nonlinear characteristics of the lift coefficient were obtained, even at low angles of attack for high-aspect-ratio wings, whereas a small lift slope and a large maximum lift coefficient were obtained for low-aspect-ratio wings. The drag and the pitching moment coefficients also exhibited nonlinear characteristics. The effect of the Reynolds number based on the wing chord was comparatively small, but a distinctive phenomenon in low-Reynolds-number flow was observed in flow visualization using oil-film and smoke-wire methods.

Nomenclature

AR	=	aspect ratio, b^2/S
a	=	lift slope
b	=	span length
c	=	chord length
$C_{( )}$	=	coefficient of forces and moment related to ( )
$\bar{c}$	=	mean aerodynamic chord
D	=	drag
D_i	=	induced drag
D_p	=	pressure drag
D_0	=	minimum drag
e	=	span efficiency factor
f	=	friction drag, frequency
k	=	proportional constant defined by Eq. (9)
K_p	=	lift slope given by lifting surface theory
K_V	=	constant value given by leading-edge suction force
K_W	=	constant value about aspect ratio of wing in blockage correction factor
L	=	lift
M	=	pitching moment
q, q_c	=	dynamic pressure and its corrected value
R	=	resultant aerodynamic force, $\sqrt{L^2 + D^2}$
r	=	distance between feathering axis and center of gravity
Re	=	Reynolds number based on $\bar{c}$
S	=	wing area
St	=	Strouhal number
S_{ts}	=	cross-sectional area of test section
t	=	wing thickness
$t/\bar{c}$	=	thickness ratio
U	=	wind velocity
α	=	angle of attack
δ	=	proportional constant defined by Eq. (9)
Δx	=	chordwise distance between quarter-chord and measurement point
Δz	=	thicknesswise model distance between measurement point and wing chord
ε	=	wall blockage correction factor
Λ	=	leading-edge sweep angle
ρ	=	air density

Subscripts

M	=	measured value
max	=	maximum value
min	=	minimum value
ST	=	strut
ts	=	test section

Introduction

WITH the development of high-speed aircraft, there have been many experimental and theoretical aerodynamic studies of various wing planforms for high-Reynolds-number ranges. Recently, the number of experimental studies for low-Reynolds-number ranges, which are pertinent to the flight of insects, has been increasing. The purpose of the present study is to investigate the aerodynamic characteristics related to the locomotion of living creatures and to the flight of small unmanned aircraft known as micro air vehicles (MAVs). Pines and Bohorquez [1] assumed that the Reynolds number for a MAV was less than 4×10^4, and they mentioned the importance of investigating the morphological and aerodynamic characteristics of the flights of creatures for developing MAVs. There have been various studies of the flapping wings of insects in flight. For example, Dickinson [2], Sunada et al. [3], and Okamoto and Azuma [4] have conducted experimental studies and Liu and Kawachi [5] and Wang [6] have performed theoretical studies of two-dimensional unsteady wings. Sane and Dickinson [7], Birch et al. [8], and Usherwood and Ellington [9,10] have conducted experimental studies and Wu and Sun [11] have performed theoretical studies of three-dimensional unsteady wings. The wing planforms used in these studies of three-dimensional wings were

Received 17 July 2009; revision received 12 November 2010; accepted for publication 8 February 2011.

*Professor, Department of Aeronautics, 7-1 Ohgigaoka, Ishikawa; okmt@neptune.kanazawa-it.ac.jp.

†Professor Emeritus, 37-3 Miyako-cho, Saiwai-Ku. Senior Member AIAA.

shaped to simulate insect wings (e.g., hawk moth, mayfly, and bumblebee). However, it is important to distinguish between two-dimensional and three-dimensional wings, because the aerodynamic characteristics of high-aspect-ratio wings are strongly affected by the wing section profile, whereas those of low-aspect-ratio wings are affected by the wing planform as well as the wing profile.

The aforementioned studies have clarified the aerodynamic characteristics of flapping wings. However, many unanswered questions still remain regarding flight at Reynolds numbers pertinent to insects, even regarding the steady state of wings. The two-dimensional characteristics of wings at $Re \leq 1 \times 10^4$ have been investigated in a wind tunnel by Okamoto et al. [12], Azuma et al. [13], and Kesel [14], and in a water tank by Sunada et al. [15]. These studies arrived at the following conclusions:

1) Streamlined airfoils intended for use at high Reynolds numbers, which have large thicknesses and leading-edge radii, exhibit poor performance due to laminar separation in flows at low Reynolds numbers, such as those for insect flight.

2) Airfoils designed for low Reynolds numbers are thin with sharp leading edges, and they sometimes have corrugated profiles like those of insect wings.

3 Lift curves at low Reynolds numbers are clearly nonlinear, whereas those at high Reynolds numbers are linear.

Various studies have been conducted on three-dimensional wings operating at low Reynolds numbers. Torres and Mueller [16] performed an experimental study of wing planforms in a wind tunnel and a water tank with a view to developing MAVs. The planforms used in their study were a rectangle and three ellipses with aspect ratios in the range $AR = 0.5$–2, and the Reynolds numbers were $(7\text{–}10) \times 10^4$. The maximum angle of attack in their experiments was below the stall angle. Cosyn and Vierendeels [17] performed a numerical analysis by computational fluid dynamics and compared the results they obtained with those of [16]. For low Reynolds numbers of $Re = 8 \times 10^3$ and 2.4×10^4, Kaplan et al. [18] tested wings with rectangular, delta shaped, and semielliptical planforms and with $AR = 2$ in a water tank. The trailing vortex was studied by digital particle velocimetry, and the calculated lift was compared with the measured lift.

The flapping wings of living creatures have high angles of attack, because such creatures require high angles of attack for their various locomotion modes. For example, Azuma [19] investigated the angles of attack that maximize the thrust of the paddling motion of duck feet and of labriform locomotion, such as that generated by the pectoral fins of fish. Suitable angles of attack are $\alpha = 40$ deg for a paddle planform with a low aspect ratio and $\alpha = 90$ deg for a paddle planform with a high aspect ratio. That is, the angle of attack at which the resultant force consisting of lift and drag is maximized is used in this locomotion. Thus, when studying the motion of creatures, aerodynamic data for steady wings have to be obtained over a wide range of angles of attack.

The purpose of the present study is to use a wind tunnel to ascertain the aerodynamic characteristics of various planforms in the vicinity of $Re = 1 \times 10^4$. The maximum angle of attack employed in this study was 90 deg. The wing planforms used in this study are elliptical, rectangular, and triangular in shape, with aspect ratios in the range $AR = 0.5$–8, a swept rectangular wing with $AR = 4$, and sweep angles of $\Lambda = 30$–60 deg. The aerodynamic characteristics of these planforms at low Reynolds numbers are compared with those at high Reynolds numbers.

The test wings were made of thin aluminum flat plate. Streamlined airfoils, such as NACA 0012, exhibit nonlinear lift curves at low Reynolds numbers [20], whereas the Reynolds number has comparatively little effect on the aerodynamic characteristics of thin flat plates. In this study, the lift and drag forces and the pitching moment acting on wings are measured, and flow visualizations by smoke-wire and oil-film methods are performed in the wind tunnel.

Preceding to the present study, Okamoto and Jinba [21] have conducted a similar experimental study. However, the test results were not satisfactory and the examination was inadequate. The present study is an extended form of preceding study.

Equipment and Experimental Method

Figure 1 shows the wind tunnel used to measure the aerodynamic forces and moment and to visualize the flow (see [12] for details). The test section is 360 mm square and 600 mm long. The wind velocity U in the test section can be varied between 2.5 and 6 m/s, and the turbulence intensity is less than 0.3%. The wind velocity is determined by counting the Kármán vortex street frequency observed downstream of the circular cylinder located in the test section (Roshko [22]).

The balance system shown in Fig. 2 consists of a load measuring device and a driving mechanism for varying the angle of attack of the wing model. The load measuring device consists of two load cells (A and B), which are aluminum blocks with four strain gauges attached to their aluminum surfaces, and they are located under the test section. Load cells A and B are used to measure, respectively, the horizontal force (or drag) and the vertical force (or lift) on the model. The driving mechanism consists of a fixed strut and a rotating sting. This sting and strut assembly is connected to the load measuring device. A small electric motor drives the sting installed on top of the strut to produce angles of attack in the range of −60 to 90 deg; this angle is measured by a potentiometer. The load measuring device, on which the model wing is set to measure the pitching moment, is installed on the tip of the sting. Device load cell C consists of a thin aluminum plate with two strain gauges attached to the aluminum surfaces. The strain gauges are connected in a bridge circuit containing two dummy gauges to compensate for temperature changes in the load cell. The load measuring device needs to be installed directly under the model, because the pitching moment acting on a wing is very small in such low-Reynolds-number flows. The respective output signals from each load cell are analyzed by a bridge circuit, a dynamic strain amplifier, and a 16-bit analog-to-digital converter, and every output is processed by a personal computer.

Aerodynamic data at various angles of attack were obtained by averaging 1500 data sets measured at a sampling frequency of 1000 Hz. An averaging time of 1.5 s was found to give sufficiently high repeatability of the output data. The minimum readable values were 9×10^{-5} N for the lift, 6×10^{-5} N for the drag, and 2×10^{-6} Nm for the moment. The maximum bias errors in the output signal were less than 0.1% for the forces and less than 0.5% for the

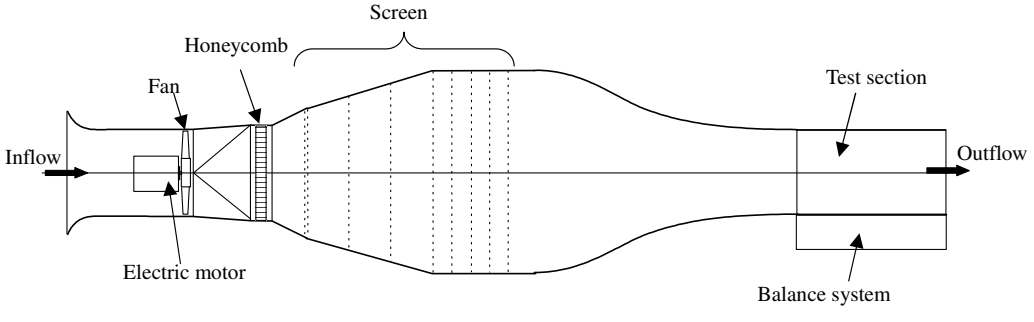

Fig. 1 Wind tunnel.

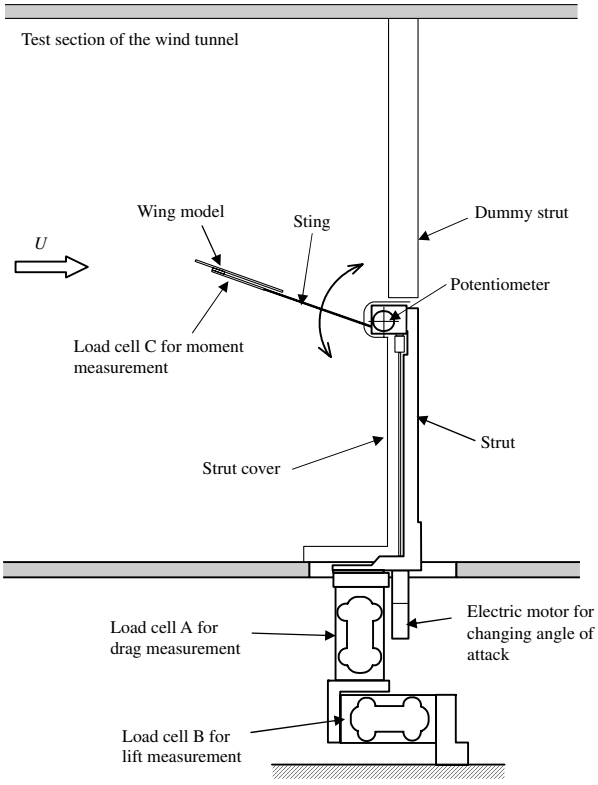

Fig. 2 Balance system.

moment over the full load range. Interference between the load cells was confirmed to be negligibly small. The natural frequencies of the load cells were more than 50 Hz for the forces and more than 180 Hz for the moment. To determine the aerodynamic forces and moment acting on the wing model, those acting on the strut and sting without the model must be subtracted from the total measured data. The mass of the models influences only the moment measurements, since it changes the position of the center of gravity. Consequently, wind-off weight tares need to be recorded and subtracted from the wind-on data. Finally, the moment about the measurement point was transferred to the quarter-chord ($0.25c$). Doing this enables the lift L, the drag D, and the moment $M_{0.25c}$ about the quarter-chord to be obtained using the following expressions:

$$L = L_{\mathrm{M}} - L_{\mathrm{ST}}, \qquad D = D_{\mathrm{M}} - D_{\mathrm{ST}}, \qquad M = M_{\mathrm{M}} - M_{\mathrm{M}(U=0)}$$
$$M_{0.25c} = M - (\Delta x_0 \cos\alpha - \Delta z_0 \sin\alpha)L - (\Delta x_0 \sin\alpha + \Delta z_0 \cos\alpha)D \tag{1}$$

where Δx_0 is the chordwise distance between the quarter-chord and the measurement point, and Δz_0 is the model thicknesswise distance from the measurement point to the chord (see Fig. 3).

By normalizing the forces and the moment with the product of the dynamic pressure $q = \frac{1}{2}\rho U^2$ and the wing area S for forces, and $S\bar{c}$ [$\bar{c}$: mean aerodynamic chord (MAC)] for the moment, nondimensional aerodynamic coefficients (the lift coefficient C_L, the drag coefficient C_D, and the moment coefficient $C_{M,0.25c}$) are given as follows:

$$C_L = \frac{L}{qS}, \qquad C_D = \frac{D}{qS}, \qquad C_{M,0.25c} = \frac{M_{0.25c}}{qS\bar{c}} \tag{2}$$

where $\bar{c}$ is given by the following equation (the chordwise positions of $0.25\bar{c}$ are indicated by the dots in Fig. 4):

$$\bar{c} = \frac{2}{S}\int_0^{b/2} c^2 \,\mathrm{d}y \tag{3}$$

Since the measured aerodynamic coefficients are considered to be affected by the blockage effect caused by the test section walls, the dynamic pressure was corrected by the classical method [23]. In this method, the blockage correction factor ε is given by

$$\varepsilon = \frac{\Delta u}{U} = \frac{S}{4S_{\mathrm{ts}}}C_{D0} + \frac{K_W S}{4S_{\mathrm{ts}}}(C_D - C_{D0} - C_{Di}) \tag{4}$$

where K_W is a constant that depends on the wing aspect ratio and S/S_{ts} is the ratio of the wing area S to the test section area S_{ts}. C_{D0} is the minimum drag coefficient, and C_{Di} is the induced drag coefficient given by $C_L^2/\pi AR$; thus, $C_D - C_{D0} - C_{Di}$ [the second term in Eq. (4)] is the drag coefficient due to flow separation.

The corrected dynamic pressure q_c is given by

$$q_c = q(1+\varepsilon)^2 \tag{5}$$

In the present experiment, S/S_{ts} varies in the range of 1.4 to 4.6%; blockage effects have very little influence at low angles of attack (i.e., $\alpha < 30$ deg), but they have noticeable influences at high angles of attack (i.e., near 90 deg).

Figure 4 shows the wing models used in this experiment. Their planforms are elliptical, rectangular (with and without a sweep angle), and triangular with various aspect ratios in the range $AR =$ 0.5 to 8. For the elliptic wings, the line of the 25% chord is a straight line, and the contours are elliptical in front of and behind the chord line.

The wing models are made of 0.5-mm-thick aluminum plates, and the shape of the wing section is rectangular with no sharp leading edges. Therefore, the thickness ratio $t/\bar{c}$ varies with the model. However, because the maximum thickness ratio of the model is small (less than 1.7%), the effect of the different thicknesses on the aerodynamic properties of the wing seems to be small [except for some slight differences in the minimum drag coefficient $C_{D\,\min}$ and

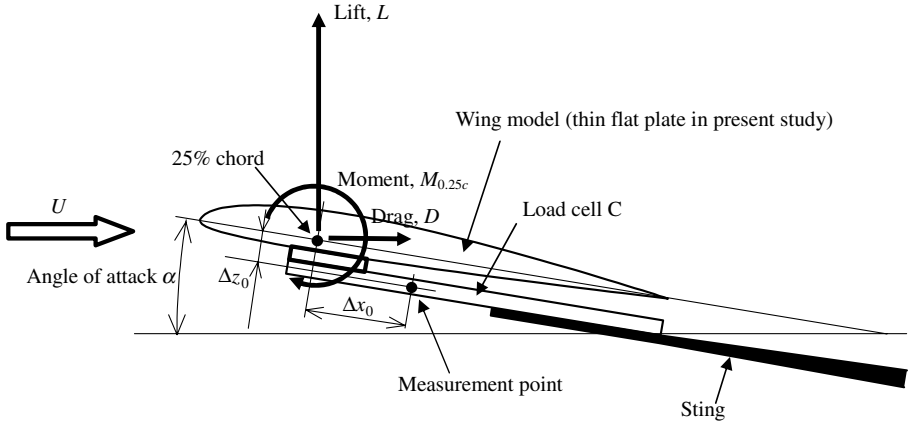

Fig. 3 Pitching moment measuring device.

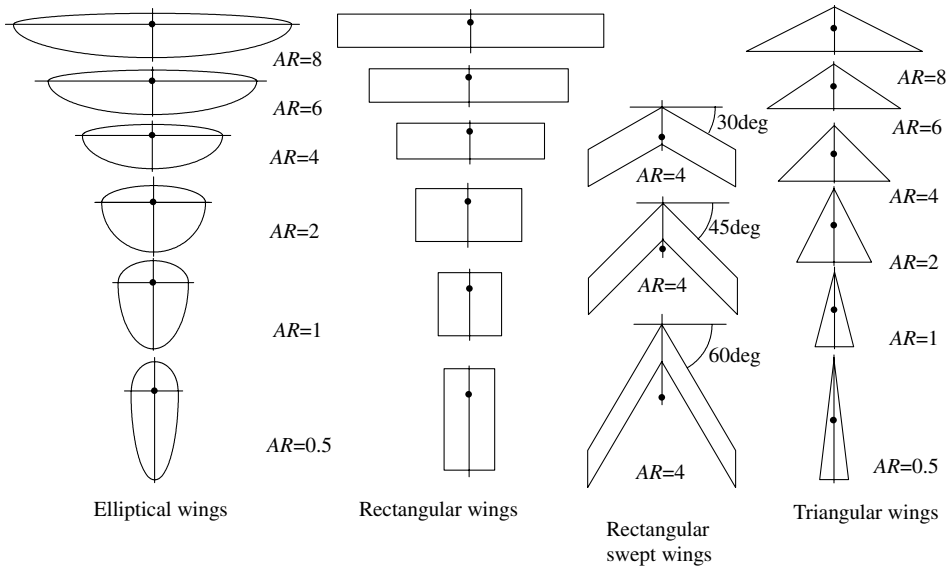

Fig. 4 Planforms of test wing models.

the maximum lift-to-drag ratio $(L/D)_{\max}$]. The wind velocity was adjusted to minimize differences between the Reynolds numbers of the wings caused by their different MAC lengths. However, due to the relatively long chords of low-aspect-ratio wings ($AR = 0.5$ for the elliptical and rectangular wings, and $AR \leq 1$ for the triangular wings), the reduction in the Reynolds number was limited.

Flow visualization techniques known as the oil-film and smoke-wire methods were conducted in low-Reynolds-number flows in the wind tunnel. In the oil-film method, a film of oil is used to observe regions of flow separation on a wing. A coat of a colored liquid paraffin was applied to the model surface, and the flow pattern was observed after a steady pattern had been obtained. To obtain suitable viscous oil flow, the viscosity of the liquid paraffin was adjusted by varying the amount of kerosene added to it.

In the smoke-wire method, smoke streamlines are generated by using an electric current to heat a wire coated with oil. The diameter of the wire used in the present study was less than 0.1 mm, and its Reynolds number was less than 30, as the flow velocity was below 4 m/s. Since the liquid paraffin on the wire evaporates as soon as the electrical current is supplied to the wire, the streak lines are instantly recorded using a high-speed movie camera at frame rates of 60–300 frames/s.

Results and Discussion

Figures 5–9 and Table 1 show the aerodynamic characteristics of the wings, with the various planforms shown in Fig. 4. Polar curves of these wings are shown in Fig. 10. The results for lift, drag, pitching moment, and resultant force coefficients are discussed in the following sections.

Lift Coefficient

Figure 5a shows the lift coefficients C_L of the elliptical wings with various aspect ratios. The lift slope of the $AR = 8$ wing is constant for angles of attack $\alpha < 8$ deg, and the C_L curve becomes almost flat, remains approximately constant within a range of 8 deg $< \alpha \leq$ 40 deg, and it then decreases to zero at $\alpha = 90$ deg. The C_L curves for wings with $AR \geq 2$ have similar shapes, and the lift slope at low angles of attack decreases as the aspect ratio decreases. In the range of aspect ratio $AR \leq 1$, the lift slope decreases, whereas C_L continues to increase to its maximum value at $\alpha \cong 45$ deg. At $AR = 1$, the maximum lift coefficient $C_{L\max}$ is about 1.5 times greater than that of wings with $AR \geq 2$. For $AR = 0.5$, $C_{L\max}$ is slightly lower than the

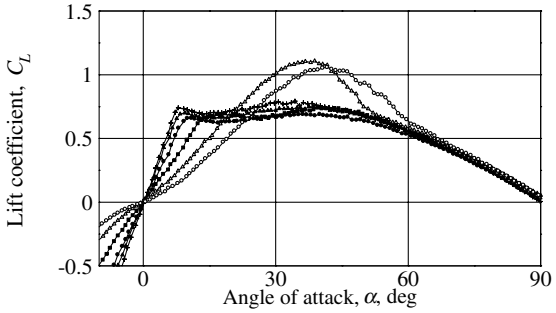

a) Lift coefficient

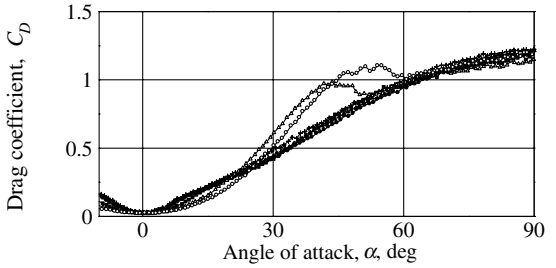

b) Drag coefficient

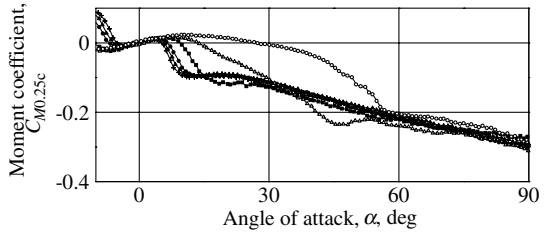

c) Moment coefficient

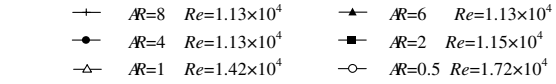

Fig. 5 Aerodynamic characteristics versus angle of attack α for elliptical wing.

value obtained for $AR = 1$. After reaching the maximum value, C_L for $AR \leq 1$ gradually decreases. In the range of $\alpha > 60$ deg, there is no noticeable difference in the shapes of the C_L curves obtained for wings with different aspect ratios.

Figure 6a shows the lift coefficients C_L of rectangular wings with various aspect ratios. The C_L curves have very similar shapes to those for the elliptical wings. The lift slope of these wings with $AR \geq 4$ is constant in the range of $\alpha < 8$ deg, but the slope gradually decreases at 8 deg, similar to the case for the elliptical wing. At $\alpha \geq 30$ deg, the C_L values of the rectangular wings with $AR \geq 6$ are slightly larger than those of wings with $AR = 2$ and $AR = 4$; this was not case for elliptical and triangular wings. For rectangular wings with $AR \leq 1$, the nonlinear lift clearly caused by the trailing vortex increases remarkably, similar to the case for the elliptical wing with the same aspect ratio.

Figure 7a shows the lift coefficient C_L of swept rectangular wings with an aspect ratio of $AR = 4$ and with sweep angles of $\Lambda = 0$ deg, 30, 45, and 60 deg. The lift slope near $\alpha = 0$ deg decreases as the sweep angle increases. However, the maximum lift coefficient increases with increasing sweep angle.

Figure 8a shows C_L of triangular wings with various aspect ratios. The linearity range of the lift curve decreases, and the lift slopes of wings with $AR \geq 4$ at $\alpha < 10$ deg are lower than those of elliptical and rectangular wings. As the aspect ratio of the triangular wing decreases, the effect of the lift slope for low-aspect-ratio wings is similar to that for other wings. However, the maximum lift coefficient $C_{L\max}$ increases dramatically to 1.14 for the $AR = 2$ wing, whereas

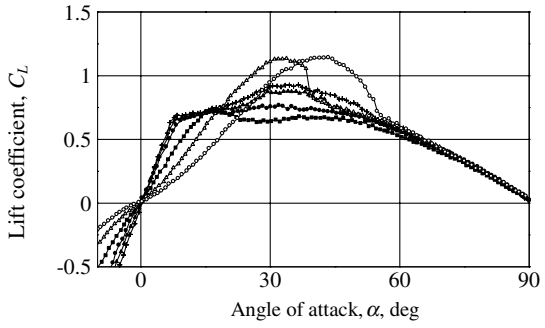

a) Lift coefficient

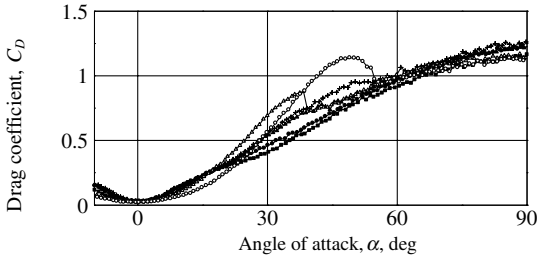

b) Drag coefficient

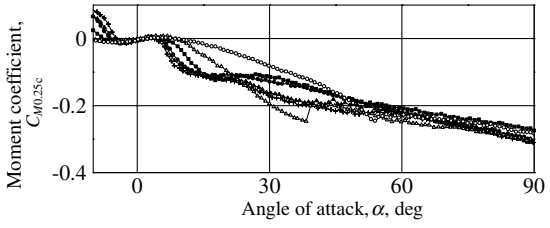

c) Moment coefficient

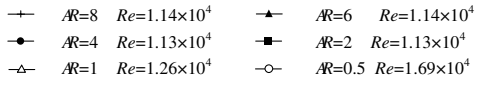

Fig. 6 Aerodynamic characteristics versus angle of attack α for rectangular wing.

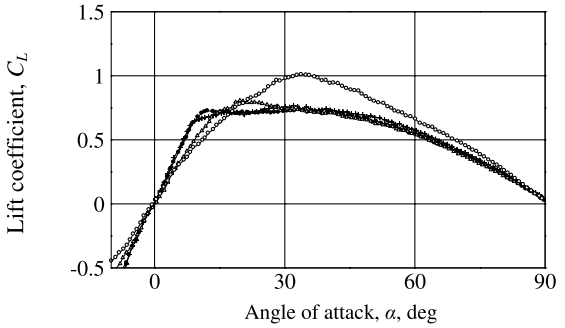

a) Lift Coefficient

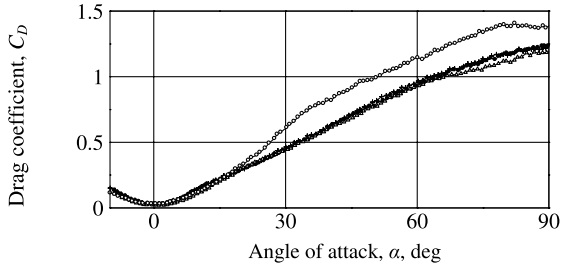

b) Drag Coefficient

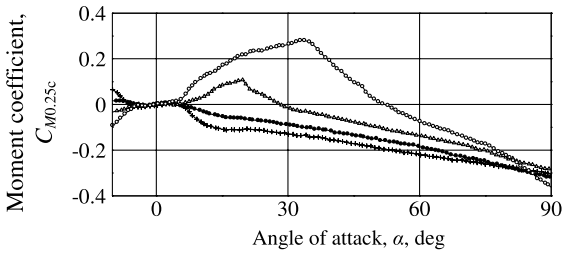

c) Moment Coefficient

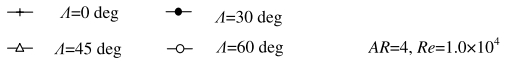

Fig. 7 Aerodynamic characteristics versus angle of attack α for rectangular swept wing.

$C_{L\max}$ for other planforms approaches its maximum value for $AR \leq 1$. Furthermore, $C_{L\max}$ of the $AR = 0.5$ wing is significantly less than that of the other planforms with the same aspect ratio.

Here, the lift slope at the angle of attack before stall and the stall characteristics are discussed.

Lift Slope

Table 2 shows the lift slopes $a = \mathrm{d}C_L/\mathrm{d}\alpha$ obtained within the angle-of-attack range -3 deg $\leq \alpha \leq 3$ deg. The lift slope a of elliptical wings with $AR \geq 4$ is larger than that of rectangular wings having the same aspect ratio. This phenomenon is clear by the traditional lifting line theory that the downwash of a elliptical wing is constant along the spanwise direction. On the other hand, in $AR \geq 2$, the lift slope a of elliptical wings is smaller than that of rectangular wings. This probably occurred because the elliptical wing has a larger thickness ratio near the tip than that of the rectangular wing. Then, the lift slopes of both triangular wings that have large taper ratios and swept wings that have large sweep angles become small for every aspect ratio. Furthermore, as the angle of attack increases over 3 deg, the lift slopes of elliptical and rectangular wings with high aspect ratios increase slightly. This is due to the vortex lift generated by the leading-edge vortex on the flat plate, as will be mentioned later.

Although the lift slope of wings with $AR \leq 1$ ($AR \geq 2$ for triangular wings) is small at -3 deg $\leq \alpha \leq 3$ deg, it increases remarkably as the angle of attack increases in $\alpha \leq 20$ deg because of the additional vortex lift by the wingtip vortices (longitudinal

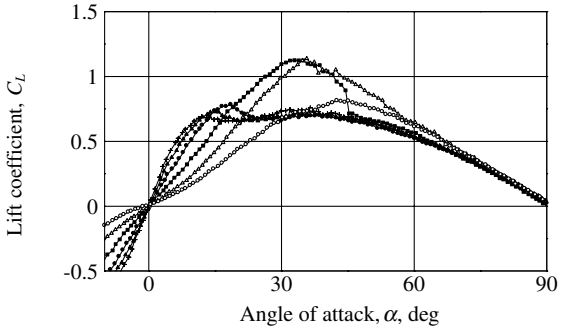

a) Lift coefficient

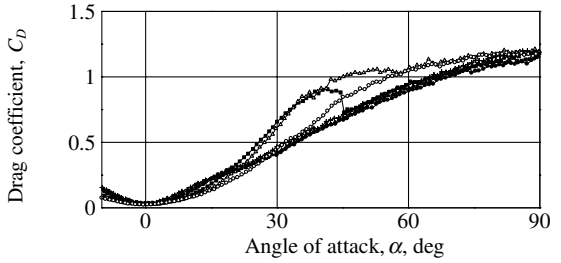

b) Drag coefficient

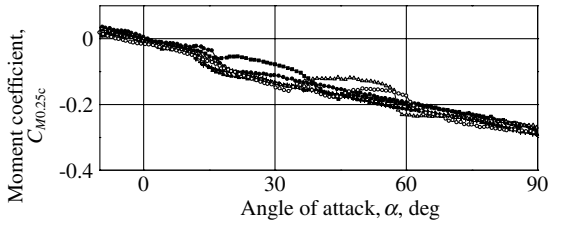

c) Moment coefficient

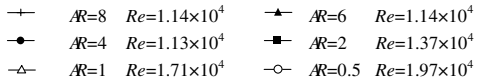

Fig. 8 Aerodynamic characteristics versus angle of attack α for triangular wing.

leading-edge vortices for triangular wings) . However, when the angle of attack increases further, the pressure distribution of the wing surface tilts backward, and the increment of a lift becomes gradually small.

The lift slope of the swept wing with a large sweep angle of $\Lambda = 60$ deg becomes small as the angle of attack increases, but $C_{L\max}$ becomes large, such as those in the case of low-aspect-ratio wings. This favorable phenomenon is believed to be resulted from the leading-edge flow separation, where the flow rolls up into a spanwise vortex (this is similar to the case of a triangular wing, discussed next).

Stalling Characteristics

When the angle of attack of high-aspect-ratio wings increases beyond the stall angle, the lift curve becomes flat. This lift curve is mainly caused by the characteristics of the thin rectangular airfoil, and the stall occurs at the small angle of attack $\alpha < 10$ deg. However, there is a little difference in the shapes of the lift curves of the different planforms. Some different shapes in stall patterns of these planforms are caused by the dissimilar spanwise pressure distributions. In the case of elliptical wings, the flow separation occurs at the same time along any spanwise station. In contrast, it occurs at the wing root for rectangular wings, and the maximum lift coefficient remains constant above the stall angle.

In the lift curve of the wings with $AR \leq 1$ ($AR \leq 2$ for triangular wings), which have large $C_{L\max}$, as the angle of attack increases beyond the stall angle, the phenomenon of the sudden decrease of C_L is seen in the rectangular wing with $AR = 1$ and the triangular wing with $AR = 2$. The lift coefficients in other wings (elliptical wings with $AR = 1$ and 0.5, rectangular wing with $AR = 0.5$, and triangular wings with $AR = 1$ and 0.5, respectively) are decreased gradually as the angle of attack increases. A sharp drop in C_L shows that the attached flow by the tip vortices suddenly separates from the wing surface. This phenomenon coincides with the line pattern, which disappears at $\alpha = 40$ deg in the oil-film study of rectangular $AR = 1$ wing, as will be mentioned later. At this point, the aerodynamic forces and moment exhibit hysteresis when the angle of attack α increases or reduces by about 1 deg. Other planforms of wing did not exhibit this characteristic in this experiment. The aerodynamic hysteresis is considered to be little in such low-Reynolds-number flows.

Drag Coefficient

The minimum drag coefficients $C_{D\min}$ ($\alpha = 0$ deg) of all wings examined (see Figs. 5b, 6b, 7b, and 8b) are very similar with each

Table 1 Aerodynamic characteristics of three wing planforms

									α, deg		
Wing planform	AR	Λ, deg	$t/\bar{c}$%	Re ($\times 10^4$)	$C_{L\max}$	$C_{D\max}$	$C_{R\max}$	$(L/D)_{\max}$	$C_{L\max}$	$C_{R\max}$	$(L/D)_{\max}$
Ellipse	8	——	1.47	1.13	0.78	1.23	1.23	7.2	36	90	4.5
	6	——	1.47	1.13	0.75	1.21	1.21	6.7	38	90	4.6
	4	——	1.47	1.13	0.69	1.19	1.19	6.4	36	90	4.6
	2	——	0.98	1.15	0.74	1.18	1.18	5.5	39	90	4.5
	1	——	0.82	1.42	1.11	1.15	1.45	4.6	38	41.1	5.7
	0.5	——	0.49	1.72	1.06	1.18	1.46	3.3	42	46.3	9.9
Rectangle	8	0	1.67	1.14	0.93	1.26	1.26	7.1	34	90	4.9
	6	0	1.67	1.14	0.88	1.22	1.22	6.6	34	90	4.0
	4	0	1.67	1.13	0.77	1.22	1.22	6.4	32	90	4.4
	2	0	1.48	1.13	0.74	1.17	1.17	5.3	18	90	4.4
	1	0	1.00	1.26	1.14	1.16	1.40	3.7	34	35.6	6.8
	0.5	0	0.50	1.69	1.14	1.15	1.57	3.4	43	47.1	9.7
Swept rectangle	4	30	1.67	1.00	0.76	1.25	1.25	6.5	33	90	4.4
	4	45	1.67	1.00	0.82	1.20	1.20	6.0	23	90	4.8
	4	60	1.67	1.00	1.01	1.41	1.43	4.9	34	79.8	4.6
Triangle	8	26.6	1.67	1.14	0.76	1.20	1.20	6.1	37	90	4.0
	6	33.7	1.67	1.14	0.73	1.18	1.18	5.8	36	90	5.2
	4	45	1.00	1.13	0.78	1.15	1.15	5.4	19	90	3.7
	2	63.4	0.83	1.37	1.14	1.16	1.42	4.5	33	38.6	7.7
	1	76.0	0.67	1.71	1.14	1.20	1.44	3.3	36	42.2	7.6
	0.5	82.9	0.57	1.97	0.81	1.17	1.22	2.4	43	55.4	13.0

other and slightly greater than twice the skin friction drag coefficient C_f calculated by using $C_f = 1.328/\sqrt{Re}$. The drag coefficients C_D of high-aspect-ratio wings are greater than those of low-aspect-ratio wings of AR ≤ 2 (AR ≤ 4 for triangular wings) at angles of attack of $\alpha < 20$ deg. This is due to the large pressure drag C_{Dp}, which is larger than the induced drag C_{Di} of high-aspect-ratio wings with rectangular airfoils, as mentioned later in the section titled "Comparison with Theory". However, in 30 deg $< \alpha < 60$ deg, the C_D of low-aspect-ratio wings becomes larger than that of high-aspect-ratio wings due to C_{Di} increased by the large C_L. Similar C_D values for $\alpha > 60$ deg are obtained for all planforms, except for the swept wing with $\Lambda = 60$ deg and triangular wings with $AR \leq 1$, both of which have slightly higher values. These results of C_D correspond to the characteristics of C_L at $\alpha > 60$ deg.

As seen in Table 1, $C_{D\max}$ ($\alpha = 90$ deg) lie in the range 1.15–1.26, except for the swept wing with $\Lambda = 60$ deg, which has an exceptionally high $C_{D\max}$ of 1.41. This high $C_{D\max}$ is similar to C_D of the rectangular flat plate with $AR = 16$ setting vertically in the flow. For such flat plates, C_D increases evidently as its aspect ratio increases over 10 (Hoerner [24]). This high $C_{D\max}$ for the highly swept wing seems to be due to its planform being equivalent to a pair of rectangular plates of $AR = 8$ arranged in a diagonal configuration.

The wing operating at high angles of attack over 60 deg becomes a bluff body with a perfectly separated flow. At $\alpha > 60$ deg, the drag coefficient of the wing obtained by using the projection area $S \sin\alpha$ instead of the wing area S was almost constant with a change in the angle of attack α. Therefore, C_L and C_D are expressed as follows:

$$C_L = C_{D\max}\cos\alpha \qquad C_D = C_{D\max}\sin\alpha \quad \text{where, } \alpha > 60 \text{ deg} \quad (6)$$

Figure 9 shows an example of the comparison between the experimental C_L and C_D and the theoretical values calculated by Eq. (6) at $\alpha > 60$ deg. It is recognized that the theory shows a near value to the experiment.

Figure 10 shows polar curves. The slopes of the tangential lines from the origin to each of these polar curves was used to obtain the maximum lift-to-drag ratio $(L/D)_{\max}$. As seen in Table 1, $(L/D)_{\max}$ increases and the angle of attack of $(L/D)_{\max}$ decreases as the aspect ratio increases. The maximum value of $(L/D)_{\max}$ obtained in this study is about seven; this value decreases as the aspect ratio decreases. The angle of attack at $(L/D)_{\max}$ is high for elliptical and rectangular wings with $AR \leq 1$ and for triangular wings with $AR \leq 2$.

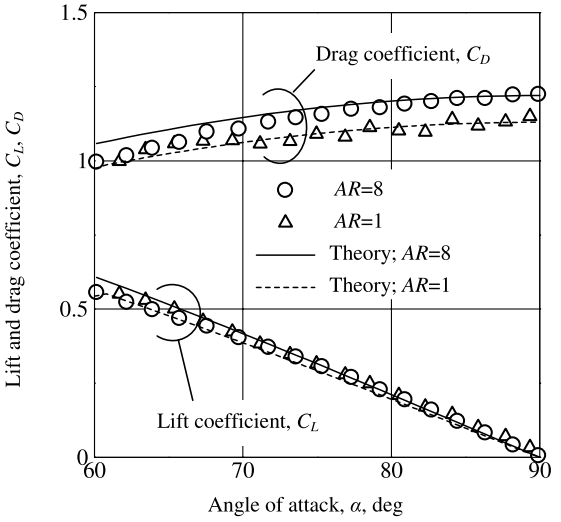

a) Elliptical wings with AR=8 and AR=1

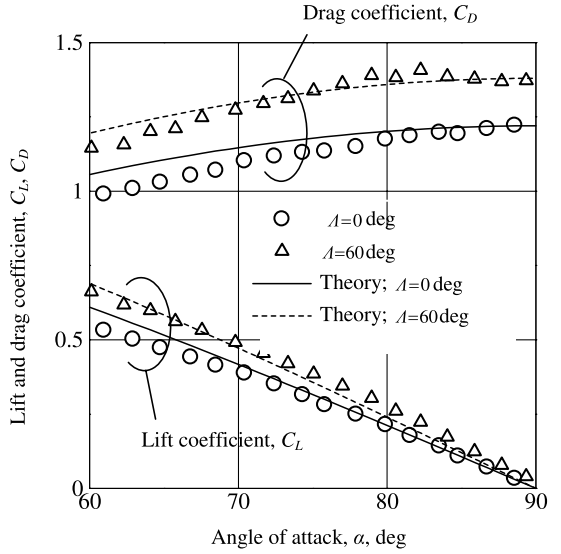

b) Rectangular swept wings with Λ = 0 deg and Λ = 60 deg

Fig. 9 Comparison of theoretical and experimental C_L and C_D at high angle of attack of $\alpha > 60$ deg.

Pitching Moment Coefficient

Figures 5c, 6c, 7c, and 8c show the pitching moment coefficient $C_{M,0.25c}$ at the 25% chord. As Figs. 5c and 6c show, the moment slopes of the elliptical and rectangular wings are nearly zero at small angles of attack, although they have slightly positive values. $C_{M,0.25c}$ becomes negative as the lift increases. $C_{M,0.25c}$ changes rapidly for high-aspect-ratio wings but gradually for low-aspect-ratio wings. These changes are related to the different lift slopes for wings with different aspect ratios. Specifically, $C_{M,0.25c}$ of the elliptical $AR = 0.5$ wing decreases the most gradually with an increasing angle of attack, and the range of the angle of attack of $C_{M,0.25c}$ near zero is larger than those of the other elliptical and rectangular wings. Figure 6c shows that there is a sudden increase in the moment of the rectangular wing with $AR = 1$ at $\alpha = 45$ deg; this abrupt change corresponds to rapid decreases in the lift and drag.

Figure 7c shows that, for the swept wings, the positive slope range of the pitching moment around $\alpha = 0$ deg extends to an angle of attack of $\alpha = 40$ deg as the sweep angle increases. This must be caused by partial flow separation or stall at the outer spanwise station near the wingtips. For the rectangular swept wing in the range of $\Lambda \geq 45$ deg, $C_{M,0.25c}$ is a maximum at the same value of α as $C_{L\max}$. For $\alpha > 40$ deg, the slope of the pitching moment $C_{M,0.25c}$ becomes large and negative.

The moment slope of the triangular wing shown in Fig. 8c is negative in the vicinity of $\alpha = 0$ deg, and the differences in the moment slopes for wings with different aspect ratios are comparatively small. As the angle of attack increases, the pitching moment variation becomes complicated for the triangular wing. When the angle of attack further increases to $\alpha > 60$ deg, $C_{M,0.25c}$ is very similar for all the planforms studied, and it decreases to nearly -0.3 at $\alpha = 90$ deg. The minimum $C_{M,0.25c}$ was obtained for the swept wing with $\Lambda = 60$ deg, and its value was -0.35. That is, the center of pressure of every wing at $\alpha = 90$ deg is located at nearly 50% of MAC, so that $C_{M,0.25c}$ is nearly equal to $-C_D/4$.

Resultant Aerodynamic Force Coefficient

The resultant aerodynamic force coefficient C_R is expressed as a nondimensional resultant force given by $C_R = \sqrt{C_L^2 + C_D^2}$. Graphically, C_R is considered to be the distance from the origin to the data points of the polar curve. As Figs. 10a–10d show, the maximum resultant force $C_{R\max}$ occurs at $\alpha = 90$ deg for high-aspect-ratio wings, whereas it occurs near $\alpha = 40$ deg for low-aspect-ratio wings. Table 1 and Fig. 10 show $C_{R\max}$ calculated using the measured values of C_L and C_D. $C_{R\max}$ is larger than $C_{D\max}$ for elliptical and rectangular wings with an aspect ratio $AR \leq 1$ (Figs. 10a and 10b, respectively) and for the triangular wing with $AR \leq 2$ (Fig. 10d). The rectangular wing with $AR = 0.5$ produced the largest $C_{R\max}$ of 1.57 of the wing models tested. The angle of attack of $C_{R\max}$ tends to increase with decreasing aspect ratio (if the value for 90 deg for $AR \geq 2$ in Table 1 is disregarded).

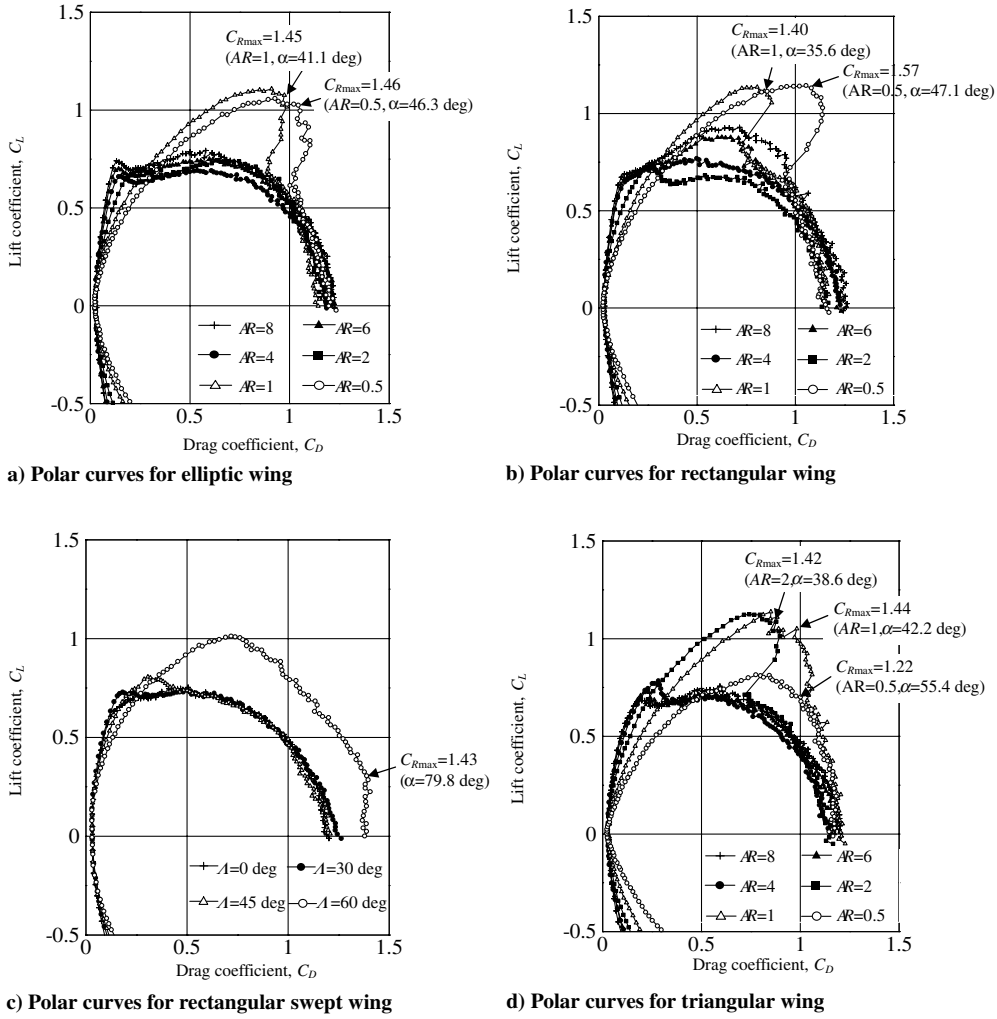

a) Polar curves for elliptic wing

b) Polar curves for rectangular wing

c) Polar curves for rectangular swept wing

d) Polar curves for triangular wing

Fig. 10 Polar curves of four wing planforms.

The $C_{R\max}$ of the swept wing with $AR = 4$ (Fig. 10c) occurs at $\alpha = 90$ deg for the wings with $\Lambda = 30$ and 45 deg, whereas it occurs at $\alpha = 79.8$ deg for the wing with $\Lambda = 60$ deg. This is because C_D for the wing with $\Lambda = 60$ deg is approximately constant for $\alpha \geq 79.8$ deg. C_R near $\alpha = 40$ deg for the swept wing with $\Lambda = 60$ deg is larger than those of the other planforms with the same aspect ratio ($AR = 4$). The next highest angle of attack for $C_{R\max}$ for the models tested was 55.4 deg for the triangular wing model with $AR = 0.5$.

Effect of Reynolds Number

In the present study, there was a limit to give the same Reynolds number of the tests for various planforms that have different lengths of MAC. Therefore, the effect of the Reynolds number on the aerodynamic characteristics in the vicinity of $Re = 1 \times 10^4$ were examined for representative planform models with high and low aspect ratios. Reynolds number effects were observed for angle of attacks $\alpha < 20$ deg for high-aspect-ratio wing models and for $\alpha < 50$ deg for low-aspect-ratio models. Reynolds number effects were not obvious at angles of attack higher than $\alpha = 60$ deg.

High-Aspect-Ratio Wing

Figure 11 shows the results obtained from the elliptical wing with $AR = 6$ by varying the Reynolds number between 0.58×10^4 and 1.3×10^4. The lift slope at $\alpha < 6$ deg is nearly constant, but it increases slightly at higher angles of attack. The nonlinearity of the lift curve seems to be due to the additional vortex lift generated by the leading-edge separation vortex. Crompton and Barett [25] revealed the existence of a leading-edge separation bubble on a sharp-edged flat plate by measuring the velocity and the pressure distribution throughout the bubble along the plate in a low-Reynolds-number range from 1×10^4 to 55×10^4. The nonlinearity of the C_L curve at $Re = 0.58 \times 10^4$ is more remarkable, and the lift slope exceeds the theoretical value for the two-dimensional lift slope of 2π. The effect

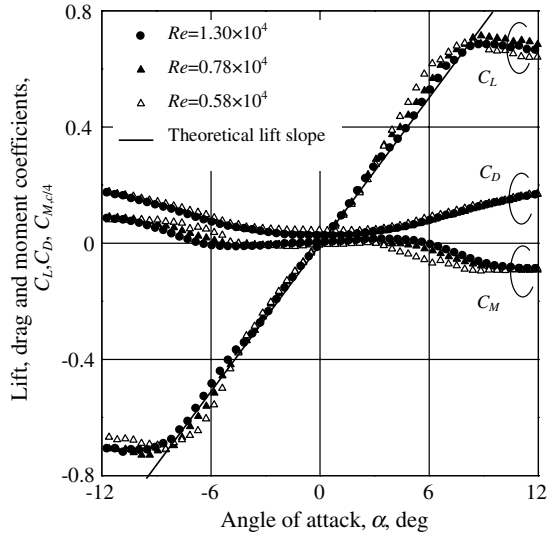

Fig. 11 Reynolds number effects on aerodynamic characteristics of elliptical $AR = 6$ wing model.

of the Reynolds number is clearly seen in the pitching moment $C_{M,0.25c}$; it changes to negative at lower angles of attack as the Reynolds number decreases. In conclusion, for high-aspect-ratio wings, the Reynolds number slightly changes the lift slopes. The wing with an airfoil profile section is considered to be more sensitive to changes in the Reynolds number. However, since the present results were obtained by using models of thin flat plates with rectangular profiles, the Reynolds number effects on the aerodynamic characteristics were little.

Low-Aspect-Ratio Wing

Figures 12–14 show the Reynolds number effects on the aerodynamic forces and moment for low-aspect-ratio wings (elliptical wing with $AR = 1$, rectangular wing with $AR = 1$, and triangular wing with $AR = 2$, respectively). The Reynolds number in the present study varied from about 1×10^4 to 2×10^4. Both the lift slope and the maximum lift coefficient $C_{L\max}$ of the wings decreased slightly with the Reynolds number in this range. This phenomenon is more pronounced for the triangular wing than for the elliptical and rectangular wings. In Fig. 13, a sharp hollow in C_L is observed at $\alpha = 40$ deg: the angle of attack at which the hollow point decreases as the Reynolds number decreases. In low-aspect-ratio wings, the stall angle decreases as the Reynolds number decreases. That is, it seems that the flow that is held on the wing surface by the wingtip vortices separates early from the wing surface by the reduction of Reynolds number.

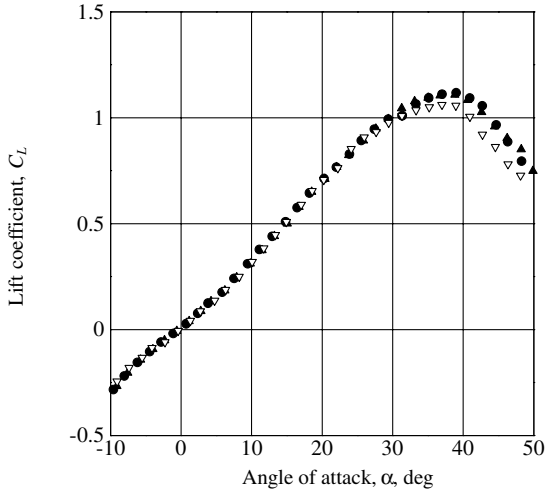

a) Lift coefficient

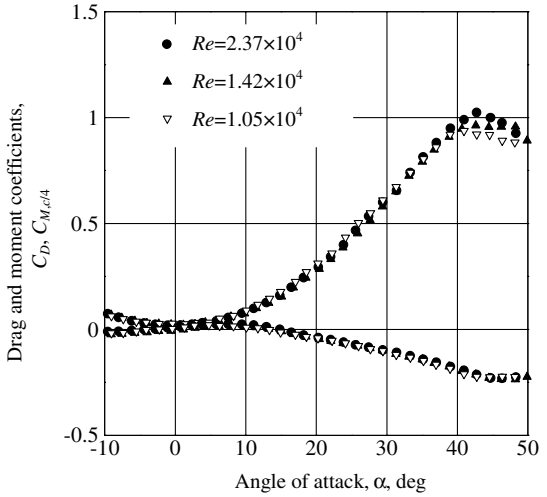

b) Drag and moment coefficients

Fig. 12 Reynolds number effects on aerodynamic characteristics of elliptical $AR = 1$ wing model.

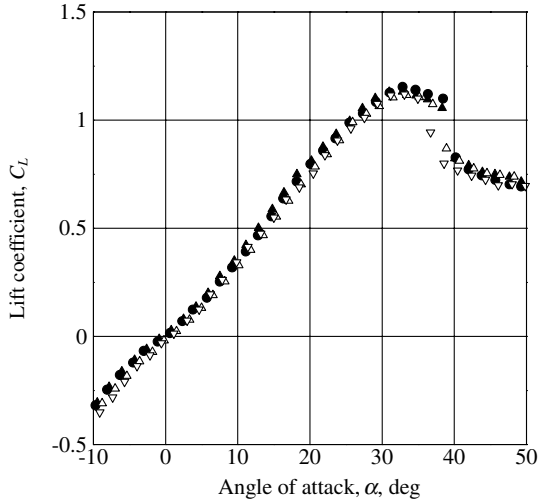

a) Lift coefficient

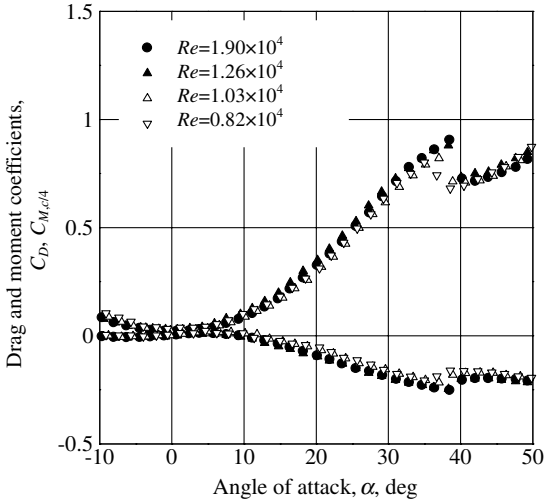

b) Drag and moment coefficients

Fig. 13 Reynolds number effects on aerodynamic characteristics of rectangular $AR = 1$ wing model.

Comparison with Theory

Many theoretical methods have been proposed for analyzing wing planform characteristics, and their accuracies have been confirmed by experimental results at high Reynolds numbers. Figure 15 shows a comparison between the experimental lift slope in Table 2 and the theoretical value calculated by the lifting surface theory of the vortex lattice method (VLM) [26]. The theoretical lift slope may be equivalent to the value of K_P, which is given later by Eq. (7). The experimental lift slopes exceed the theoretical values for high-aspect-ratio wings, but they agree with each other quite well for low-aspect-ratio wings (except for the experimental data for the elliptical wing, which are slightly lower than theoretical predicted values). The leading-edge separation of the rectangular cross section started at very low angles of attack, and it must be the cause of the discrepancies in the lift slopes. The lift slope of high-aspect-ratio wings reduces when the leading edge is made sharp or the wing section thickness decreases. In the thin flat plate with a sharp leading edge, the lift slope at $\alpha < 2$ deg is small due to laminar separation. In contrast, the lift slope becomes large for -3 deg $< \alpha < 3$ deg for the rectangular leading edge, since the separation occurs at a smaller α and the vortex lift contributes to the lift due to the leading-edge vortex. On the other hand, the effect of the thickness of the airfoil section seems to be small for low-aspect-ratio wings. For the swept wings, both experimental and theoretical lift slopes exhibit a similar trend, such that they decrease as the sweep angle increases for a given aspect ratio.

There is a method for calculating the nonlinear lift coefficient of low-aspect-ratio wings in classical theory. For triangular wings, a vortex generated from the apex to the trailing edge along the swept leading edge generates vortex lift, and the lift slope increases as the angle of attack increases. Polhamus [27,28] modeled this phenomenon by setting the vortex lift to be equal to the leading-edge suction force calculated by potential theory. That is, the direction of the leading-edge suction force vector turns from horizontal to vertical by the flow separation at a sharp leading edge, and this vortex lift contributes to the lift augmentation (Polhamus' leading-edge suction analogy). The lift coefficient C_L based on this approach is given by

$$C_L = K_P \sin\alpha\cos^2\alpha + K_V \sin^2\alpha\cos\alpha \tag{7}$$

where K_P is the lift slope given by the lifting surface theory, K_V is estimated from the leading-edge suction force, and the vortex lift is obtained by multiplying $K_V \sin^2\alpha$ by $\cos\alpha$. K_P and K_V are presented as functions of the aspect ratio. By assuming no leading-edge suction due to vortex lift, the drag coefficient C_D is given by

$$C_D = C_L \tan\alpha + C_{D0} \tag{8}$$

where C_{D0} corresponds approximately to twice the skin friction drag C_f.

For rectangular wings, Lamar [29] showed that the vortex lift can be calculated by using the suction analogy for leading-edge and side-edge suction forces. The results have been confirmed by experimental results for sharp-edged rectangular and triangular wings at high Reynolds numbers of $Re > 10^6$. Table 3 shows K_P and K_V for triangular and rectangular wings with low-aspect-ratio planforms.

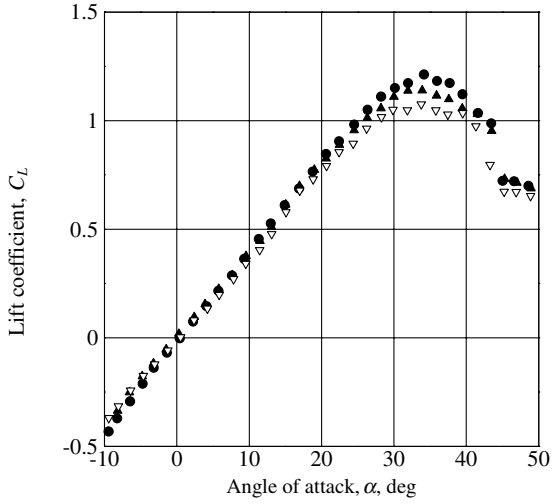

a) Lift coefficient

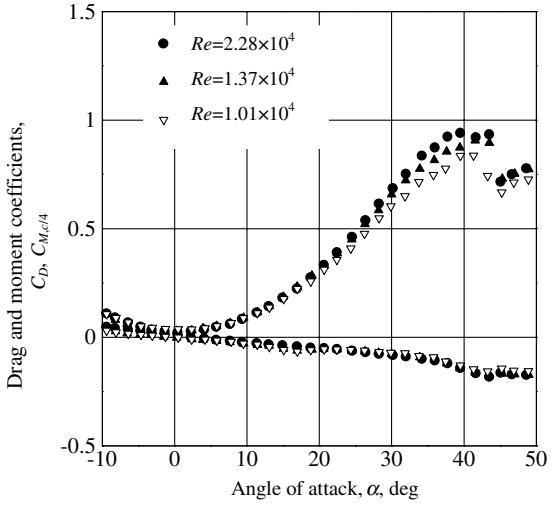

b) Drag and moment coefficients

Fig. 14 Reynolds number effects on aerodynamic characteristics of triangular $AR = 2$ wing model.

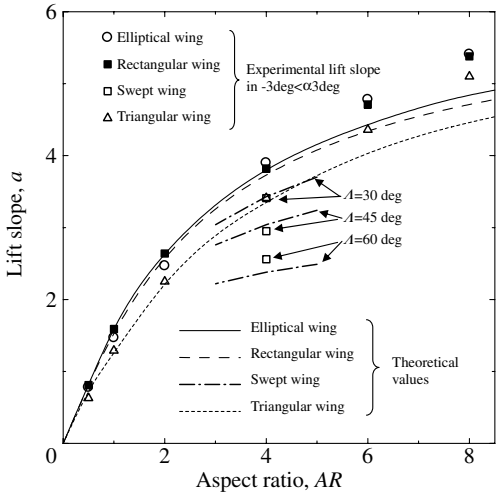

Fig. 15 Experimental and theoretical lift slopes versus different aspect ratios.

Theoretically computed C_L and C_D characteristics are represented by solid lines for $AR = 1$ and dashed lines for rectangular and triangular wings with $AR = 0.5$ in Figs. 16 and 17a, respectively. In the angle-of-attack range -10 deg $\leq \alpha \leq 25$ deg, the experimentally measured C_L and C_D of rectangular wings with $AR = 1$ and 0.5 agree well with the theoretical results (Fig. 16), whereas the measured values for the triangular wing are lower than the computational results over a wide angle-of-attack range. Since the influence of the thickness at the leading edge is considered to be the cause of this discrepancy between the experimental and calculated results, tests were conducted of a triangular wing with $AR = 2$ with a sharp leading edge. In this case, there was a very small difference between the results for rectangular and sharp leading edges, as seen in Fig. 17b. Because the effects of the Reynolds number on the triangular wing are larger than those of the other two planforms (see Fig. 14), we tentatively change the value of K_V in Eq. (7) from 3.1 to half this value; when this is done, the theoretical lift slope agrees well with the experimental results (Fig. 17b). Therefore, it seems to be that the leading-edge vortex lift seems to decrease at low Reynolds numbers.

Figure 18 shows a comparison of the drag coefficients among experimental and calculated results based on Eq. (8) and the potential theory based on the induced drag $C_{Di} = C_L^2/\pi ARe$, which is mentioned later in the range of angle of attack $\alpha < 60$ deg. It is recognized that 1) the experimental results coincide well with the calculated C_D given by Eq. (8); and 2) the induced drag coefficient calculated from the potential theory is small, specifically in high-aspect-ratio wings. The same results were obtained in all planforms of the wings tested. That is, the pressure drag is larger than the induced drag in wings that have thin rectangular airfoils.

From these results, it is considered that $C_D - C_{D0}$ is in proportion to the squared angle of attack a^2 in the linear range of the C_L curve, where C_{D0} is the drag coefficient at $C_L = 0$ and equal to $C_{D\min}$ in the experiment. Therefore, the drag coefficient C_D is able to be expressed as follows:

$$C_D = C_{D0} + k\alpha^2 = C_{D0} + C_{Dp} + C_{Di} = C_{D0} + \delta\alpha^2 + \frac{C_L^2}{\pi ARe} \tag{9}$$

where C_{Dp} is the pressure drag coefficient that seems to be in proportion with a^2, δ is the proportional constant, and C_{Di} is the induced drag coefficient in which e is the span efficiency factor and is $e = 1$ for the elliptical lift distribution. The theoretical C_{Di} was obtained by calculating the downwash at the 25% chord of the wing element by the wing surface theory of VLM, and the value of e was

Table 2 Experimental lift slope of wing in angle-of-attack range $-3 \text{ deg} \le \alpha \le 3 \text{ deg}$

				Swept rectangle		
AR	Ellipse	Rectangle	Triangle	$\Lambda = 30$ deg	$\Lambda = 45$ deg	$\Lambda = 60$ deg
8	5.41	5.38	5.10	——	——	——
6	4.78	4.71	4.36	——	——	——
4	3.90	3.82	3.41	3.41	2.95	2.56
2	2.47	2.64	2.25	——	——	——
1	1.47	1.59	1.29	——	——	——
0.5	0.78	0.81	0.63	——	——	——

Table 3 K_P and K_V values for triangular and rectangular wings with low aspect ratios [23–25].

	Rectangular wing		Triangular wing	
AR	0.5	1	1	2
K_P	0.77	1.46	1.31	2.22
K_V	2.93	2.91	3.16	3.20

obtained by using the theoretical C_{Di}. At the present low Reynolds number, it is unknown that the potential theory is applicable. However, since the effect of the Reynolds number of the wings with thin rectangular airfoils is comparatively small, as stated before, this theory may be used this time.

Figure 19 shows the proportional constants k and δ versus the aspect ratio of the wing, obtained from the experimental results that are expressed in the quadratic equations of the angle-of-attack range less than the stall angle. The applicable range of angle of attack for each wing is as follows:

1) For $AR = 8$, $\alpha = 6$ deg; for $AR = 6$, $\alpha < 7$ deg; and for $AR = 4$, $\alpha = 8$ deg.

2) For $AR = 2$, $\alpha = 10$ deg for the elliptical and rectangular wings, and $\alpha = 30$ deg for the triangular wing.

3) For $AR = 1$, $\alpha < 30$ deg; and for $AR = 0.5$, $\alpha = 30$ deg.

4) For $\Lambda = 30$ deg, $\alpha = 10$ deg; for $\Lambda = 45$ deg, $\alpha = 20$ deg; and for $\Lambda = 60$ deg, $\alpha = 30$ deg for the swept wings.

In high-aspect-ratio wings, the k value, which shows the size of $C_D - C_{D0}$, is larger than that of low-aspect-ratio wings due to the differences in lift slopes. In the same aspect ratio wings, the k of the elliptical wing is the largest and is slightly small for the rectangular wing, and it is the smallest for the triangular wing. This is caused by the lift slope a, which is the largest for the elliptical wing and the smallest for the triangular wing, as seen in Table 1. In low-aspect-ratio wings, the difference of k in planforms with the same aspect ratio is small. As the sweep angle of the swept wing increases, k decreases due to the reduction in the lift slope.

The δ value, which shows the ratio of the pressure drag coefficient C_{Dp} to C_D, increases as the aspect ratio decreases. From these results, it is recognized that the difference of the induced drag in the different aspect ratio of the wing is comparatively small, and the pressure drag of high-aspect-ratio wings is larger than that of low-aspect-ratio wings. As the sweep angle of the swept wing increases, the δ value increases. This is due to the small induced drag C_{Di} resulting from both the small lift slope and the large aspect ratio of the swept wing with large sweep angles. This phenomenon is different from the results of low-aspect-ratio wings, which are affected by the separation vortex of the leading edge similarly.

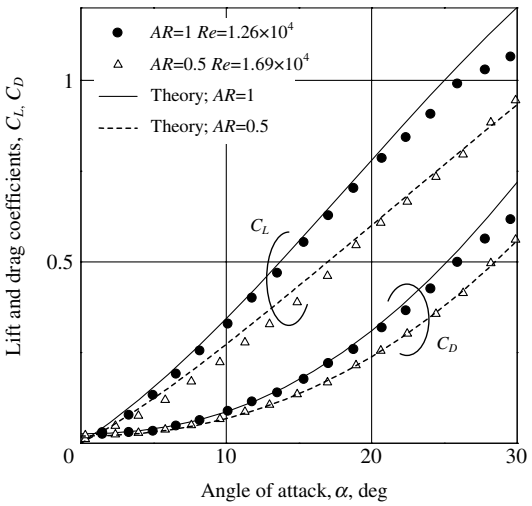

Fig. 16 Comparison of theoretical and experimental aerodynamic force coefficients of low-aspect-ratio rectangular wings.

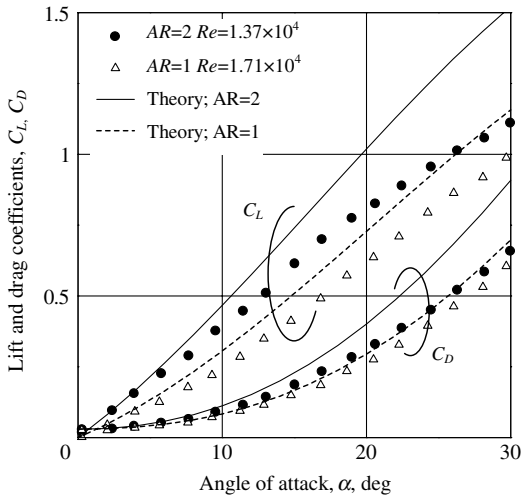

a) Comparison of experimental data with the theory of Refs. [25,26]

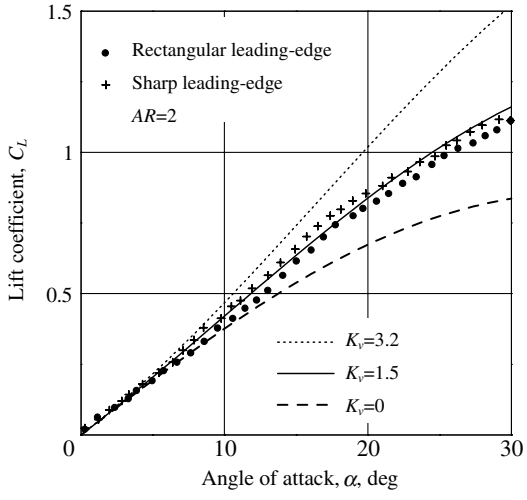

b) Effect of different values of K_v in Eq. (7).

Fig. 17 Comparison of theoretical and experimental aerodynamic forces coefficients of low-aspect-ratio triangular wing.

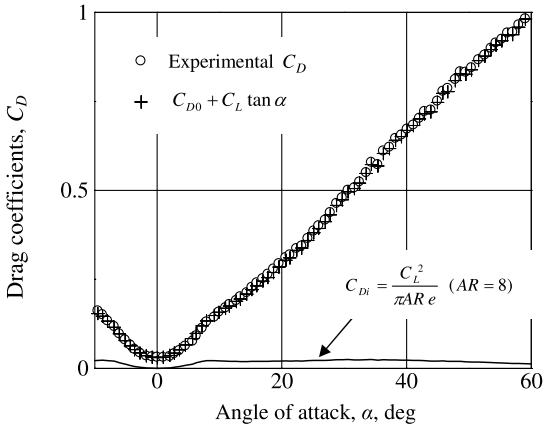

a) C_D of elliptical wing with AR=8

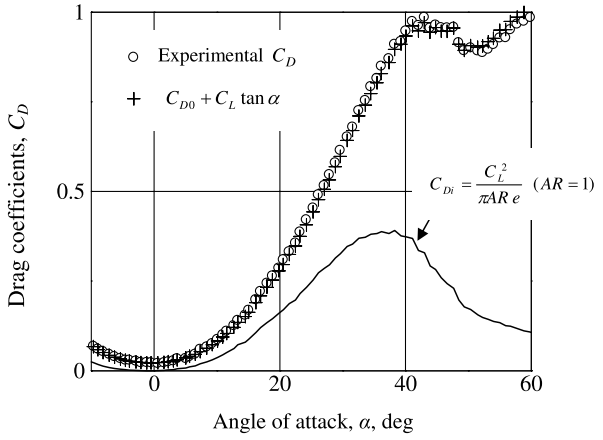

b) C_D of elliptical wing with AR=1

Fig. 18 Comparison of theoretical C_D by Eq. (8) and experimental C_D in elliptical wing.

Flow Pattern on Wing Surface

The oil-film method was used to visualize the flow separation region on the wing surface. The oil film on the wing surface becomes dark in the region where the flow in the boundary layer reverses its direction, and it becomes light where the flow is in the general direction around the model. Figure 20 shows the results for oil flow on the elliptical wing with $AR = 6$. The line-shaped pattern seen in Fig. 20a appears on the wing surface at about the 30% chord at an angle of attack of $\alpha = 6$ deg. This seems to be caused by a separation

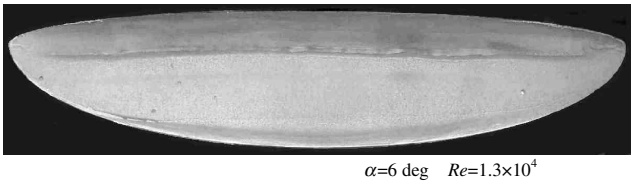

a) Typical oil-flow patterns

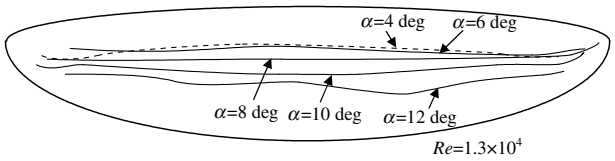

b) Variation of line patterns

Fig. 20 Oil-flow pattern for elliptical $AR = 6$ wing.

vortex generated on the leading edge of the wing. Figure 20b shows that the line pattern moves to nearly the 60% chord as the angle of attack increases. This pattern is still visible at $\alpha = 12$ deg, although the lift slope is small, but it disappears at $\alpha = 15$ deg.

Figure 21 shows the results of the oil-flow study on the elliptical wing with $AR = 1$. In Fig. 21a, a line pattern is seen near the leading edge of the wing at $\alpha = 10$ deg. It moves downstream at $\alpha =$ 20 deg. This pattern moves slightly forward at $\alpha = 30$ and 40 deg (Fig. 21b), and it disappears at $\alpha = 50$ deg, where the wing stalls completely. The line pattern moves toward the trailing edge as the Reynolds number decreases.

Figure 22 shows the results of oil-flow study for the rectangular wing with $AR = 1$. The line pattern visible near the leading edge of the wing at $\alpha = 5$ deg shifts backward and splits into two components, which move to the opposite wingtips at $\alpha \cong 10$ deg and prevent flow separation at the wingtips. At $\alpha = 30$ deg, the oil pattern spreads from nearly the 40–50% chord of the wing to the trailing edge. The line pattern, which curves to the trailing edge at $\alpha = 35$ deg, moves slightly forward, and it is not seen at $\alpha = 40$ deg. It moves toward the trailing edge as the Reynolds number decreases. This trend is similar to that for the elliptical wing.

Figure 23 shows the oil-flow results for the triangular $AR = 2$ wing. Since the longitudinal vortex along the leading edge appears on the upper surface of the triangular wing at every positive angle of attack, the line pattern that corresponds to the vortex appears from the apex to the trailing edge of the wing. Hoerner and Borst [30] showed that the large leading-edge vortex induced strong lateral flow toward the edge and generated a small secondary vortex. The thin line

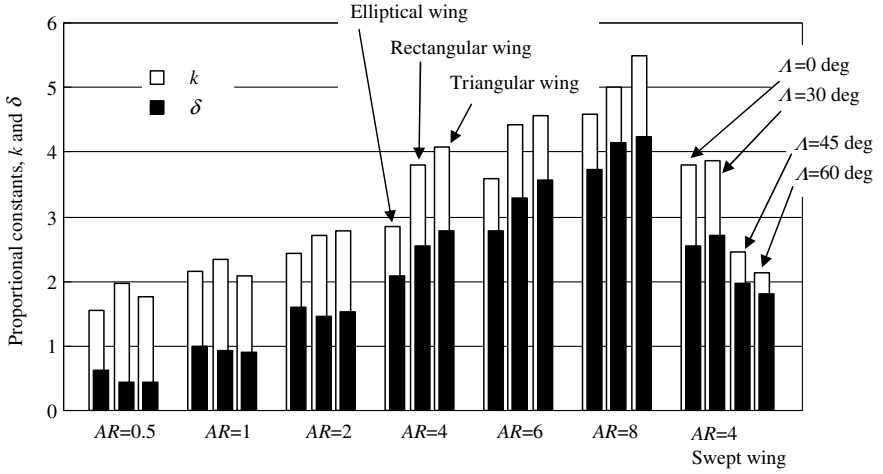

Fig. 19 Proportional constants k and δ versus aspect ratio AR.

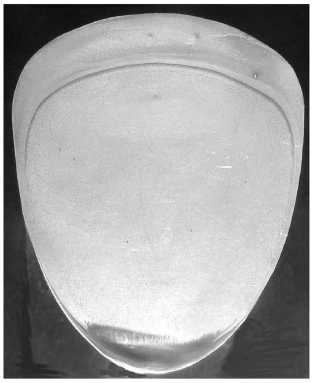

α=10 deg Re=2.4×10^4

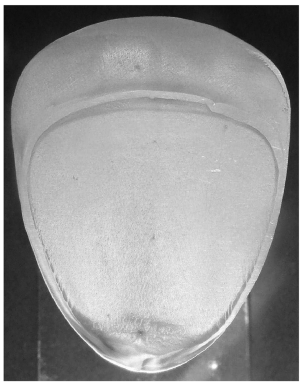

α=10 deg Re=1.4×10^4

a) Typical oil-flow patterns

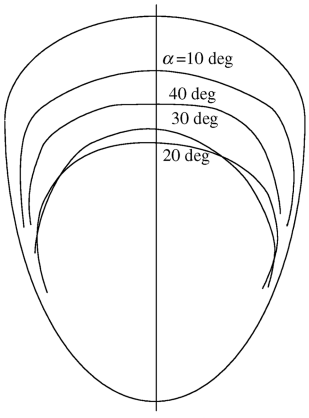

Re=2.4×10^4

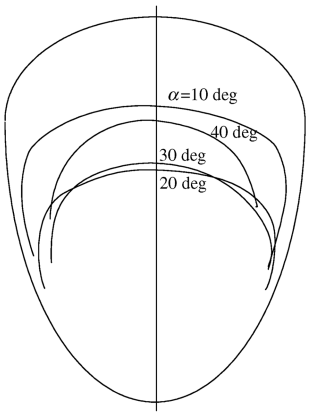

Re=1.4×10^4

b) Variation of line patterns

Fig. 21 Oil-flow patterns for elliptical $AR = 1$ wing.

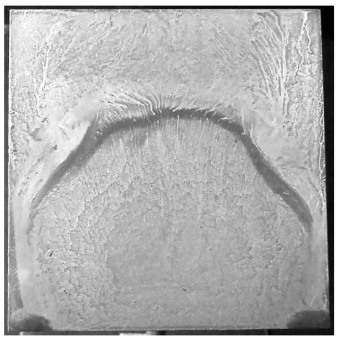

α=30 deg Re=1.9×10^4

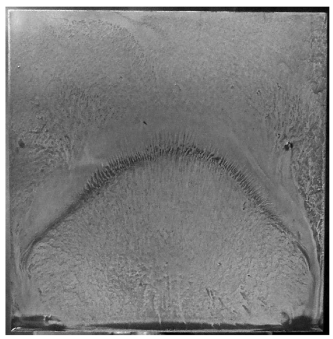

α=30 deg Re=1.0×10^4

a) Typical oil-flow patterns

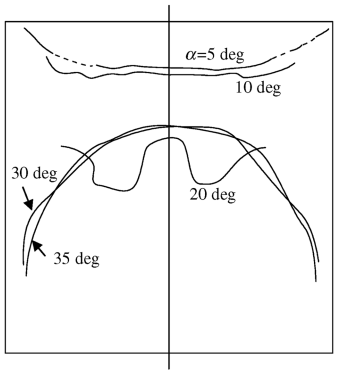

Re=1.9×10^4

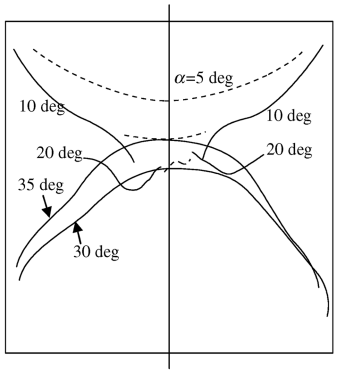

Re=1.0×10^4

b) Variation of line patterns

Fig. 22 Oil-flow patterns for rectangular $AR = 1$ wing.

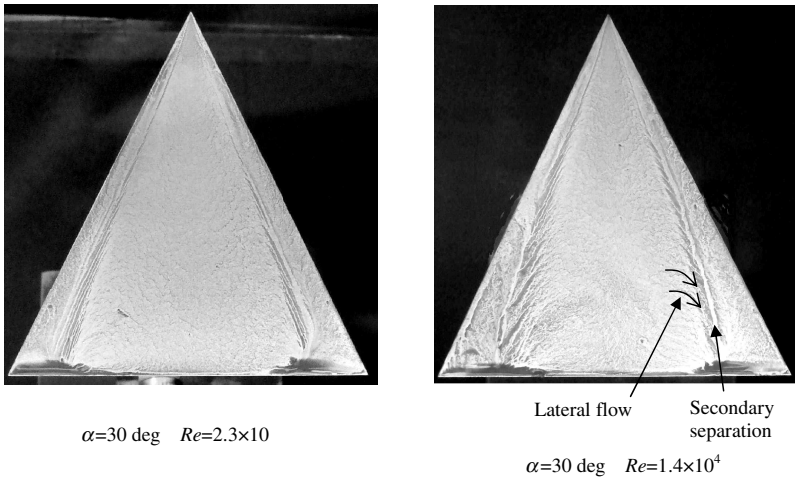

a) Typical oil-flow patterns

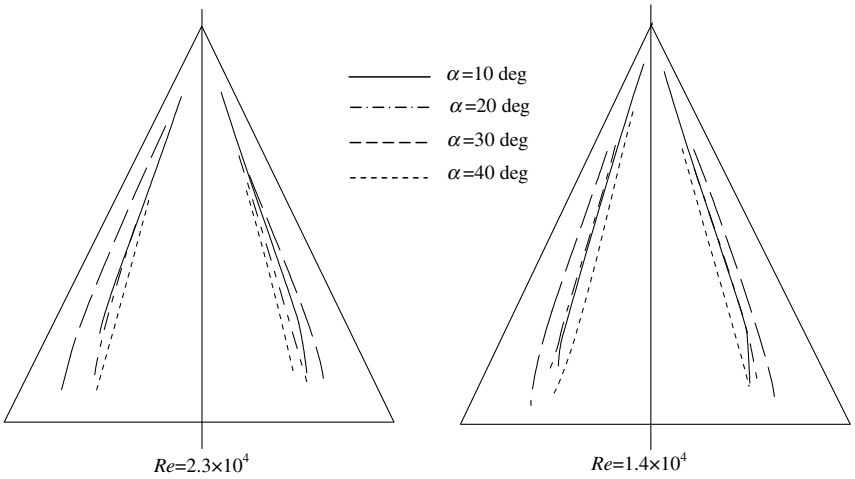

b) Variation of line pattern

Fig. 23 Oil-flow pattern for triangular $AR = 2$ wing.

in Fig. 23a shows the reattachment line for the leading-edge vortex. The lines in Fig. 23b represent the separation lines of lateral flow. The line patterns observed for $\alpha = 10$ and 20 deg move toward the leading edge at $\alpha = 30$ deg, but they move toward the center of the wing at $\alpha = 40$ deg.

The oil-film results reveal that there are some differences in the oil-film patterns with a change in the Reynolds number; however, the differences in the forces and moment acting on the wing were comparatively small, as stated previously.

Flow Visualization Around the Wing

In addition to the oil-film study, flow visualization by the smoke-wire method was conducted. Figure 24 shows photographs of the streak lines that were obtained by generating smoke lines at an upstream station on the midspan of the elliptical wing with $AR = 1$. The instantaneous visualization results obtained by the smoke-wire method are difficult to compare with the results for the average force measurements and the oil-flow patterns for the mean flow. However, the line pattern of the oil-film method will appear as a fixed vortex on the wing surface when the vortex remains there for a long time. The separation vortex is observed on the leading edge of the wing at $\alpha = 10$ deg, and small vortices generated from its leading-edge vortex shed to the rear. Torres and Mueller [16] described the reattachment of a separation bubble generated at the leading edge of low-aspect-ratio rectangular wings using a thin flat plate in their study at $Re = 7\text{–}10 \times 10^4$. In the present study, reattachment of the separated flow could not be clearly observed due to the presence of small unsteady vortices shed from the rear part of the leading-edge vortex. However, the line pattern at small α shown in Figs. 20–22 must be generated along the stagnation line between the reverse flow and the forward flow following the leading-edge vortex. The size of the leading-edge vortex increases very little with increasing α. Figure 25 depicts the behavior of vortices on a typical flat-plate wing surface. Many small vortices are shed to the rear, and reverse flow on the wing surface is observed near the leading edge. All vortices rotate clockwise when viewed from the left tip. The generation frequency of the small shedding vortices is about $f = 100$ Hz at $Re = 1 \times 10^4$, and it is independent of the angle of attack. The Strouhal number St defined by $St = fc \sin\alpha / U$ is about $St = 0.4$ at $\alpha = 10$ deg. A large vortex can also be seen off the trailing edge of the wing in Figs. 24 and 25. This large vortex appears at a frequency of about 10 Hz ; it engulfs some of the other small vertices near the center of the chord, and it flows to the rear. These vortices are seen at larger angles of attack.

At $\alpha = 20$ deg, many small vortices separate from the wing surface and are shed from the trailing edge, but the remaining vortices are caught by a pair of large tip vortices and flow away with them. Another vortex is seen under the many small shedding vortices (see Fig. 25). The line pattern at $\alpha = 20$ deg (Fig. 21) must be due to the reverse flow caused by the vortex on the surface near the midchord of the model. At $\alpha = 30$ deg for the elliptical wing with $AR = 1$, the space between the small vortices and the wing surface widens, but the lift is still large at this high angle of attack.

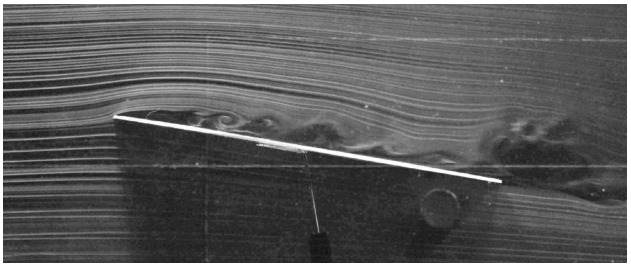

α=10 deg

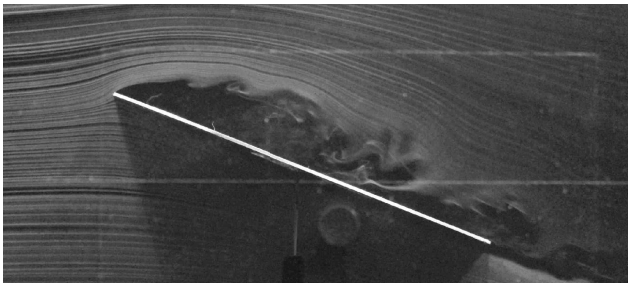

α=20 deg

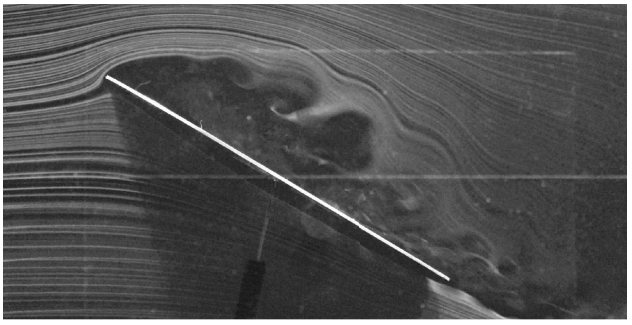

α=30 deg

Fig. 24 Flow visualization at midspan of elliptical $AR = 1$ wing at $Re = 1.0 \times 10^4$.

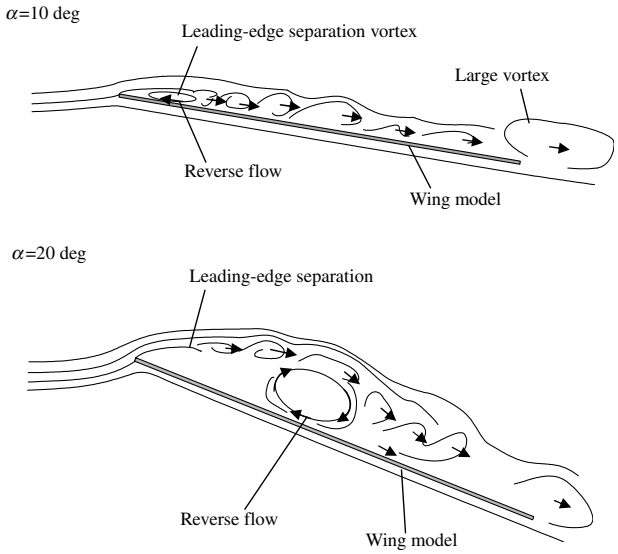

Fig. 25 Behavior of vortices in Fig. 24.

Conclusions

The following results are obtained from the wind-tunnel tests of various wing planforms at low Reynolds numbers of around 1×10^4:

1) It is confirmed at high Reynolds numbers ($Re \geq 10^6$) that the experimental results coincide with those given by the VLM and leading-edge suction analogy based on the potential theory. At low Reynolds numbers ($Re \cong 10^4$) in the present study, the effect of Reynolds number on the aerodynamic forces acting on the three-dimensional wing profiled with a thin rectangular airfoil is comparatively small, except the triangular wing with the aspect ratio of $AR \leq 2$. As a result, the lift slope generally decreased with the reduction of the aspect ratio, whereas the $C_{L\max}$ of the wing with $AR = 1$ ($AR = 2$ for triangular wings) was about 1.5 times as large as that of higher-aspect-ratio wings.

2) However, in the small range of the Reynolds number of $0.58 \times 10^4 \leq Re \leq 2.37 \times 10^4$, there was a little change in the lift slope of high-aspect-ratio wings and in the lift curve near the maximum lift coefficient $C_{L\max}$ for low-aspect-ratio wings. That is, when the Reynolds number decreased, a) nonlinearity of the lift slope of high-aspect-ratio wings was more remarkable due to the leading-edge vortex, b) $C_{L\max}$ of low-aspect-ratio wings slightly decreased, and c) the C_L of the triangular wing with $AR \leq 2$ became smaller than the theoretical value due to the longitudinal leading-edge vortices.

3) In low-Reynolds-number flows, it was confirmed by the flow visualization that the leading-edge separation vortex could not reattach on the wing surface and many small vortices flowed out from the separated region.

4) In the drag coefficients C_D of the wings with thin rectangular airfoils, the pressure drag is larger than the induced drag, specifically in high-aspect-ratio wings. Because of the large pressure drag, the C_D of high-aspect-ratio wings is larger than that of low-aspect-ratio wings at small angles of attack. However, as the angle of attack increases, the C_D becomes large for low-aspect-ratio wings due to the induced drag increased by the large C_L.

5) At $\alpha > 60$ deg, the differences in the aerodynamic characteristics of the different planforms are comparatively small. However, for the swept wing with a large sweep angle of $\Lambda \geq 60$ deg, C_L and C_D are slightly larger than those of the other planforms. The maximum drag coefficient $C_{D\max}$ obtained at $\alpha = 90$ deg is nearly 1.2 for all wings tested, except the swept wing with $\Lambda = 60$ deg, for which $C_{D\max}$ was 1.41. This high $C_{D\max}$ for the swept wing with large sweep angle seems to be caused by its configuration, which is considered to be a pair of the slim rectangular plates arranged diagonally.

6) The maximum resultant aerodynamic force coefficient $C_{R\max}$ occurs at $\alpha = 90$ deg for high-aspect-ratio wings, whereas it appeared near $\alpha = 40$ deg for low-aspect-ratio wings. The rectangular $AR = 0.5$ wing had a maximum resultant force $C_{R\max}$ of 1.57, which was the largest value of the models examined.

7) Because every tested airfoil was rectangular, the pitching moment coefficient $C_{M,0.25c}$ at the 25% chord around $\alpha = 0$ deg was nearly zero for all wings tested. The slopes of $C_{M,0.25c}$ are slightly positive at small angles of attack for all wings, except for the triangular wing, which is negative; for the swept wings with large sweep angles, the positive moment slopes extend to large angles of attack. These slopes change to negative as the angle of attack increases, and the minimum pitching moment $(C_{M,0.25c})_{\min}$ occurs at $\alpha = 90$ deg. The center of pressure at $\alpha = 90$ deg was located near 50% of the MAC for all wings tested.

Acknowledgments

The authors are grateful to Shojiro Shindo for his support in writing this paper. They are also grateful to Yoshiki Jimba and Yasuhiro Tabata in the advanced course at Akita National College of Technology for their assistance in conducting the experiments.

References

[1] Pines, D. J., and Bohorquez, F., "Challenges Facing Further Micro-Air-Vehicle Development," *Journal of Aircraft*, Vol. 43, No. 2, 2006, pp. 290–305.
doi:10.2514/1.4922

[2] Dickinson, M. H., "The Effects of Wing Rotation on Unsteady Aerodynamic Performance at Low Reynolds Numbers," *Journal of Experimental Biology*, Vol. 192, No. 1, 1994, pp. 179–206.

[3] Sunada, S., Kawachi, K., Matsumoto, M., and Sakaguchi, A., "Unsteady Force on a Two-Dimensional Wing in Plunging and Pitching Motions," *AIAA Journal*, Vol. 39, No. 7, 2001, pp. 1230–1239. doi:10.2514/2.1458

[4] Okamoto, M., and Azuma, A., "Experimental Study on Aerodynamic Characteristics of Unsteady Wings at Low Reynolds Number," *AIAA Journal*, Vol. 43, No. 12, 2005, pp. 2526–2536. doi:10.2514/1.14813

[5] Liu, H., and Kawachi, K., "Leading-Edge Vortices of Flapping and Rotary Wings at Low Reynolds Number," *Fixed and Flapping Wing Aerodynamics for Micro Air Vehicle Applications*, edited by T. J. Mueller, Vol. 195, Progress in Astronautics and Aeronautics, AIAA, Reston, VA, 2001, pp. 275–285.

[6] Wang, Z. J., "Two Dimensional Mechanism for Insect Hovering," *Physical Review Letters*, Vol. 85, No. 10, 2000, pp. 2216–2219. doi:10.1103/PhysRevLett.85.2216

[7] Sane, S. P., and Dickinson, M. H., "The Aerodynamic Effects of Wing Rotation and a Revised Quasi-Steady Model of Flapping Flight," *Journal of Experimental Biology*, Vol. 205, 2002, pp. 1087–1096.

[8] Birch, J. M., Dickson, W. B., and Dickinson, M. H., "Force Production and Flow Structure of Leading Edge Vortex on Flapping Wings at High and Low Reynolds Numbers," *Journal of Experimental Biology*, Vol. 207, No. 7, 2004, pp. 1063–1072. doi:10.1242/jeb.00848

[9] Usherwood, J. R., and Ellington, C. P., "The Aerodynamics of Revolving Wings. I. Hawkmoth Wings," *Journal of Experimental Biology*, Vol. 205, 2002, pp. 1547–1564.

[10] Usherwood, J. R., and Ellington, C. P., "The Aerodynamics of Revolving Wings. II:. Propeller Force Coefficient from Mayfly to Quail," *Journal of Experimental Biology*, Vol. 205, 2002, pp. 1565–1576.

[11] Wu, J. H., and Sun, M., "Unsteady Aerodynamic Forces of Flapping Wing," *Journal of Experimental Biology*, Vol. 207, No. 7, 2004, pp. 1137–1150. doi:10.1242/jeb.00868

[12] Okamoto, M., Yasuda, K., and Azuma, A., "Aerodynamic Characteristics of the Wings and Body of a Dragonfly," *Journal of Experimental Biology*, Vol. 199, No. 2, 1996, pp. 281–294.

[13] Azuma, A., Okamoto, M., and Yasuda, K., "Aerodynamic Characteristics of Wing at Low Reynolds Number," *Fixed and Flapping Wing Aerodynamics for Micro Air Vehicle Applications*, edited by T. J. Mueller, Vol. 195, Progress in Astronautics and Aeronautics, AIAA, Reston, VA, 2001, pp. 341–398.

[14] Kesel, A. B., "Aerodynamic Characteristics of Dragonfly Wing Sections Compared With Technical Aerofoils," *Journal of Experimental Biology*, Vol. 203, No. 20, 2000, pp. 3125–3135.

[15] Sunada, S., Yasuda, T., Yasuda, K., and Kawachi, K., "Comparison of Wing Characteristics at an Ultralow Reynolds Number," *Journal of Aircraft*, Vol. 39, No. 2, 2002, pp. 331–338. doi:10.2514/2.2931

[16] Torres, G. E., and Mueller, T. J., "Aerodynamic Characteristics of Low Aspect Ratio Wings at Low Reynolds Numbers," *Fixed and Flapping Wing Aerodynamics for Micro Air Vehicle Applications*, edited by T. J. Mueller, Vol. 195, Progress in Astronautics and Aeronautics, AIAA, Reston, VA, 2001, pp. 115–141.

[17] Cosyn, P., and Vierendeels, J., "Numerical Investigation of Low-Aspect-Ratio Wings at Low Reynolds Numbers," *Journal of Aircraft*, Vol. 43, No. 3, 2006, pp. 713–722. doi:10.2514/1.16991

[18] Kaplan, S. M., Altman, A., and Ol, M., "Wake Vorticity Measurements for Low Aspect Ratio Wings at Low Reynolds Number," *Journal of Aircraft*, Vol. 44, No. 1, 2007, pp. 241–251. doi:10.2514/1.23096

[19] Azuma, A., *The Biokinetics of Flying and Swimming*, 2nd ed., AIAA Education Series, AIAA, Reston, VA, 2006, pp. 387–434.

[20] Ohtake, T., Nakae, Y., and Motohashi, T., "Nonlinearity of the Aerodynamic Characteristics of NACA0012 Airfoil at Low Reynolds Numbers," *Journal of the Japan Society for Aeronautical and Space Sciences*, Vol. 55, No. 644, 2007, pp. 439–445. doi:10.2322/jjsass.55.439 (in Japanese).

[21] Okamoto, M., and Jinba, Y., "Experimental Study on Aerodynamic Characteristics of Wing Planforms at Low Reynolds Number," *Research Reports of Akita National College of Technology*, No. 44, 2009, pp. 42–50 (in Japanese).

[22] Roshko, A., "Experiments on the Flow Past a Circular Cylinder at Very High Reynolds Numbers," *Journal of Fluid Mechanics*, Vol. 10, No. 03, 1961, pp. 345–356. doi:10.1017/S0022112061000950

[23] Shindo, S., "Simplified Tunnel Correction Method," *Journal of Aircraft*, Vol. 32, No. 1, 1995, pp. 210–213. doi:10.2514/3.46705

[24] Hoerner, S. F., *Fluid-Dynamic Drag, Practical Information on Aerodynamic Drag and Hydrodynamic Resistance*, Hoerner Fluid Dynamics, Bakersfield, CA, 1965, Chap. 3.

[25] Crompton, M. J., and Barrett, R. V., "Investigation of the Separation Bubble Formed Behind the Sharp Leading Edge of a Flat Plate at Incidence," *Proceedings of the Institution of Mechanical Engineers. Part G, Journal of Aerospace Engineering*, Vol. 214, No. 3, 2000, pp. 157–176. doi:10.1243/0954410001531980

[26] Bertin, J. J., and Smith, M. L., *Aerodynamics for Engineers*, Prentice–Hall, Englewood Cliffs, NJ, 1989, pp. 235–298.

[27] Polhamus, E. C., "A Concept of the Vortex Lift of Sharp-Edge Delta Wings Based on a Leading-Edge-Suction Analogy," NASA TN D-3767, Dec. 1966.

[28] Polhamus, E. C., "Application of the Leading-Edge-Suction Analogy of Vortex Lift to the Drag due to Lift of Sharp-Edge Delta Wings," NASA TN D-4739, 1968.

[29] Lamar, J. E., "Extension of Leading-Edge-Suction Analogy to Wing with Separated Flow Around the Side Edges at Subsonic Speeds," NASA TR R-428, 1974.

[30] Hoerner, S. F., and Borst, H. V., *Fluid-Dynamic Lift, Practical Information on Aerodynamic and Hydrodynamic Lift*, edited by H. V. Borst, 2nd ed., Hoerner Fluid Dynamics, Bakersfield, CA, 1985, Chap. 18.

A. Naguib
Associate Editor